HHS Public Access

Author manuscript

FEBS J. Author manuscript; available in PMC 2020 August 03.

Published in final edited form as:

FEBS J. 2020 March ; 287(5): 941–963. doi:10.1111/febs.15066.

Osteocytic miR21 deficiency improves bone strength independent of sex despite having sex divergent effects on osteocyte viability and bone turnover

Hannah M. Davis[1,5], **Padmini J. Deosthale**[1], **Rafael Pacheco-Costa**[1], **Alyson L. Essex**[1,5], **Emily G. Atkinson**[1,5], **Mohammad W. Aref**[1,5], **Julian E. Dilley**[1], **Teresita Bellido**[1,2,4,5], **Mircea Ivan**[3], **Matthew Allen**[1,4,5], **Lilian I. Plotkin**[1,4,5,*]

[1]Department of Anatomy & Cell Biology, Indianapolis, IN, 46202, USA.

[2]Division of Endocrinology Department of Medicine, Indiana University School of Medicine, Indianapolis, IN, 46202, USA.

[3]Division of Hematology/Oncology, Department of Medicine, Indiana University School of Medicine, Indianapolis, IN, 46202, USA.

[4]Roudebush Veterans Administration Medical Center, Indianapolis, IN, 46202, USA.

[5]Center for Musculoskeletal Health, Indianapolis, IN, 46202, USA.

Abstract

Osteocytes play a critical role in mediating cell-cell communication and regulating bone homeostasis, and osteocyte apoptosis is associated with increased bone resorption. miR21, an oncogenic microRNA, regulates bone metabolism by acting directly on osteoblasts and osteoclasts, but its role in osteocytes is not clear. Here, we show that osteocytic miR21 deletion has sex-divergent effects in bone. In females, miR21 deletion reduces osteocyte viability, but suppresses bone turnover. Conversely, in males, miR21 deletion increases osteocyte viability, but stimulates bone turnover and enhances bone structure. Further, miR21 deletion differentially alters osteocyte cytokine production in the two sexes. Interestingly, despite these changes, miR21 deletion increases bone mechanical properties in both sexes, albeit to a greater extent in males. Collectively, our findings suggest that miR21 exerts both sex-divergent and sex-equivalent roles in osteocytes, regulating osteocyte viability and altering bone metabolism through paracrine actions on osteoblasts and osteoclasts differentially in males vs. females, whereas, influencing bone mechanical properties independent of sex.

[*]**Corresponding author:** Lilian I. Plotkin, Ph.D., Department of Anatomy and Cell Biology, Indiana University School of Medicine, 635 Barnhill Drive, MS-5035, Indianapolis, IN 46202-5120. Phone: 1-317-274-5317. Fax: 1-317-278-2040. lplotkin@iupui.edu.

Contributions

Study design was performed by HMD, RPC, and LIP. Data acquisition was performed by HMD, PD, ALE, RPC, EGA, and JED. Advice on μCT analysis and biomechanical testing, and contribution of materials was performed by MRA, MI and MWA. Discussion of the findings HMD, RPC, MWA, MRA, TB, and MI. Data analysis and interpretation was performed by HMD and LIP. Drafting of manuscript was performed by HMD and LIP. All authors revised the manuscript and approved the final version.

Conflicts of Interest

The authors declare no competing interests.

Keywords

microRNA; miR21; bone; osteocyte; apoptosis; sexual-dimorphism; cytokine

Introduction

Osteocytes are the most prevalent and long-living type of cell in bone [1]. Extensive evidence suggests that osteocytes embedded in the bone matrix are targets of bone acting stimuli, and that osteocyte lifespan affects skeletal homeostasis [2-5]. Osteocytes regulate bone remodeling by modulating osteoclasts and osteoblasts through direct cell-cell interactions and via extracellular signaling through the release of soluble factors [1,6]. Additionally, osteocyte viability is reduced in conditions of increased bone fragility [7,8,4,9] and conversely, agents that preserve bone strength prevent osteocyte apoptosis [2-5]. Moreover, osteocyte apoptosis and the prevalence of empty lacunae are increased in old mice and humans [10,11]. However, the molecular mechanisms that lead to increased osteocyte apoptosis and the osteocyte-derived signaling factors that control bone metabolism in old age are not completely understood.

Recent work has identified microRNAs (miRs) as negative regulators of gene expression [12]. miRs are ~18-22-nucleotide long noncoding RNAs that regulate a plethora of cellular processes and dysregulation of particular miRs have been associated with numerous human diseases. Changes in miR expression can also contribute to the effects of aging in several organs [13]. In particular, alterations in miR21 abundance, a miR predominantly regarded as pro-survival and oncogenic, have been detected in numerous pathologies. In bone, miR21 has been shown to directly regulate osteoblast and osteoclast differentiation and function [14]. However, the role of miR21 in osteocytes and its effects on bone turnover remain unclear.

We previously demonstrated several putative pro-survival miRs are dysregulated in MLO-Y4 osteocytic cells in the absence of Cx43. In particular, miR21 levels are significantly decreased in Cx43-deficient cells, which undergo spontaneous apoptosis in culture; and addition of a miR21 mimic sufficiently restores the viability of these cells [15]. Conversely, inhibition of miR21 induces osteocyte apoptosis in control MLO-Y4 osteocytic cells. Further, we found that bones from mice lacking osteocytic Cx43 and from old female mice express lower levels of miR21 compared to control $Cx43^{f/f}$ and young mice, respectively [16]. Based on these findings and the notion that osteocyte apoptosis triggers osteoclast differentiation and recruitment [17], a simplistic model would predict apoptotic effects on osteocytes upon miR21 deletion, with subsequent increases in bone resorption and decreases bone strength. However, given the complex nature of miR regulation, both intra- and extracellular, in nearly every cell in the body, it should not have been surprising that this hypothesis was overly simplistic. Here, we provide experimental evidence that *in vivo* effects of the miR21 locus are more nuanced, and identify for the first time a sex-divergent impact of miR21 on osteocyte biology. We show that miR21 regulates osteocyte viability in a sex-dependent manner, preserving osteocyte viability in females but reducing osteocyte viability in males. Further, we demonstrate that osteocytic miR21 regulates osteocyte

cytokine production and bone turnover in a sex-specific manner. In particular, we found miR21 deletion differentially altered osteocyte cytokine production, as well as, several related signaling pathways in females and males. Despite these changes, miR21 deletion enhanced bone mechanical properties in both sexes, albeit to a greater extent in males. Taken together, these results suggest that miR21 exerts a sex-divergent role in osteocytes, regulating bone mass and architecture through non-cell autonomous effects on osteoblasts and osteoclasts, whereas, miR21 has sex-equivalent effects on bone mechanical properties.

Results

miR21 regulation of osteocyte viability and mitochondrial function is sex-dependent.

To investigate the role of osteocytic miR21 locus *in vivo*, we generated a mouse model in which miR21 was deleted from osteocytes (Fig. 1a). Targeted-deletion of miR21 in osteocytes decreased miR21 levels ~50% in calvaria bone lysates of both female and male miR21$^{\Delta ot}$ compared to control miR21$^{f/f}$ mice (Fig. 1b). On the other hand, no significant changes in miR21 levels were found in the gastrocnemius muscle of male or female mice, even though reporter studies showed that skeletal muscle expressed the Cre recombinase under the DMP1-8kb promoter [18] (not shown). Interestingly, basal miR21 levels were higher in miR21$^{f/f}$ females than males, suggesting a sex-related difference in miR21 expression in bone. Additionally, we detected decreases in mRNA levels of vacuole membrane protein-1 (VMP1) in both female and male miR21$^{\Delta ot}$ compared to control miR21$^{f/f}$ mice, due to overlap between miR21 and the 3' UTR of VMP1 (Fig. 1b). However, no sex-specific differences in VMP1 expression were detected in control mice. Further, VMP1 levels were not altered by inhibition or overexpression of miR21 in osteocytic MLO-Y4 cells (not shown), suggesting that the effect of miR21 deletion *in vivo* on RANKL/OPG levels and on cell viability are a direct consequence of reduced miR21 levels and not of changes in VMP1 expression.

Similar to our previous findings in Cx43-deficient osteocytic cells [15], in females, the RANKL/OPG mRNA ratio was increased in bones from miR21$^{\Delta ot}$ compared to miR21$^{f/f}$ mice (Fig. 1c). Additionally, female miR21$^{\Delta ot}$ mice exhibited higher expression of the apoptosis-associated gene P27, as well as tendencies towards higher Gadd153 and Foxo3 (Fig. 1d). Moreover, miR21 inhibition in control MLO-Y4 osteocytic cells, which are derived from a female mouse, increased the RANKL/OPG mRNA ratio and the expression of the apoptosis associated-genes (P27, Gadd153, and Foxo3) (Fig. 2a). Conversely, transfection of a miR21 mimic decreased the RANKL/OPG mRNA levels and apoptosis-related gene expression (Fig. 2b). Further, miR21 inhibition increased the expression of apoptosis-associated genes (Fig. 2c) whereas miR21 overexpression, attenuated the increased RANKL/OPG mRNA ratio and apoptosis associated-gene expression (Fig. 2d) in Cx43-deficient MLO-Y4 cells, which exhibit increased levels of apoptosis and express low levels of miR21 compared to scramble-silenced cells [15].

While no changes in RANKL or OPG gene expression were detected in the miR21$^{\Delta ot}$ compared to miR21$^{f/f}$ males (Fig. 1e), interestingly, our findings suggest that miR21 negatively regulates osteocyte viability. Specifically, miR21$^{\Delta ot}$ males exhibited lower levels of the apoptosis-associated genes (p27, Gadd153 and Foxo3) (Fig. 1f). Consistent with the

sex-divergent effects of osteocytic miR21 deletion on the apoptosis-associated genes and RANKL/OPG mRNA levels, miR21 deletion differentially altered mitochondrial gene expression in females and males. Specifically, miR21$^{\Delta ot}$ females, but not males exhibited significantly lower levels of several mitochondria-associated genes, whereas in males, the expression of ND2 was increased (Fig. 3a,b).

Removal of osteocytic miR21 differentially regulates bone turnover in females and males.

To determine whether removal of osteocytic miR21 also regulates bone mass and bone cell activity in a sex-dependent manner, we next examined the bone phenotype of miR21$^{\Delta ot}$ and miR21$^{f/f}$ mice of each sex. In females, deletion of miR21 from osteocytes did not alter the distribution of cartilage and mineralized bone in newborn mice (Fig. 4a). Similarly, total, spinal and femoral BMD were not affected by miR21 deletion in females up to 4 months of age, although slight increases in body weight were detected between 2 and 4 months of age in miR21$^{\Delta ot}$ compared to miR21$^{f/f}$ mice (Fig. 4b). On the other hand, in males, total, spinal and femoral BMD were all significantly increased by 4 months of age in miR21$^{\Delta ot}$ compared to miR21$^{f/f}$ mice, while body weight was unaltered (Fig. 4c).

Osteocytic miR21 deletion led to sex-specific changes in bone cell activity and bone geometry in both cortical and cancellous bone compartments. In females, dynamic bone histomorphometry analysis of the femur mid-diaphysis showed that, while the bone formation parameters on the periosteal surface were not changed, MS/BS (the mineralized surface per total bone surface) and BFR/BS (bone formation rate per bone surface) were significantly lower on the endocortical surface in miR21$^{\Delta ot}$ compared to miR21$^{f/f}$ mice (Fig. 5a). Conversely, in males, dynamic histomorphometry analysis of the femur mid-diaphysis showed that all bone formation measurements, MAR (mineral apposition rate), MS/BS, and BFR/BS, were increased on the periosteal surface, whereas no changes in bone formation were detected on the endocortical surface (Fig. 5b). Further, static histomorphometry analysis of the endocortical femur surface in females revealed a reduction in osteoclast number and surface per bone surface (N.Oc/BS and Oc.S/BS) in miR21$^{\Delta ot}$ compared to miR21$^{f/f}$ mice (Fig. 5c). Consistent with the histomorphometric findings in cortical bone, decreases in circulating serum levels of the bone turnover makers, CTX, P1NP, and ALP were also detected in the female miR21$^{\Delta ot}$ compared to miR21$^{f/f}$ mice (Fig. 6). In contrast to the reduced osteoclasts parameters in the miR21$^{\Delta ot}$ females, in males, N.Oc/BS and Oc.S/BS were higher in the miR21$^{\Delta ot}$ compared to miR21$^{f/f}$ mice (Fig. 5d).

Consistent with the sex-related alterations in bone cell activity induced by osteocytic miR21 deletion, sex-dependent changes in femur cortical bone geometry were also revealed by μCT analysis of the femur mid-diaphysis. In females, the suppressed endocortical bone turnover did not alter cortical bone geometry (Fig. 5e), whereas in males, the μCT parameters, tissue area (TA), bone area (BA), cortical thickness (C.Th), marrow cavity area, and moment of inertia were all increased in miR21$^{\Delta ot}$ compared to miR21$^{f/f}$ mice (Fig. 5f).

Sex-dependent alterations in bone turnover and architecture were also detected on cancellous surfaces within the vertebra. However, unlike the decrease in formation detected on the endocortical femur surface in females, removal of osteocytic miR21 did not alter cancellous osteoblast number or activity (Fig. 7a,b). On the other hand, reductions in Oc.S/BS were

detected on the cancellous surface of miR21$^{\Delta ot}$ compared to miR21$^{f/f}$ female mice, while N.Oc/BS was unchanged (Fig. 7c). In males, no significant changes in cancellous osteoblast number or surface per cancellous bone surface (N.Ob/BS and Ob.S/BS) were detected in miR21$^{\Delta ot}$ compared to miR21$^{f/f}$ mice (Fig. 7d). However, the dynamic histomorphometry bone formation parameter MS/BS was significantly higher in the male miR21$^{\Delta ot}$ mice, suggestive of higher amounts of bone forming surface (Fig. 7e). Similar to N.Ob/BS and Ob.S/BS, no significant differences in vertebral cancellous N.Oc/BS and Oc.S/BS were detected in the male miR21$^{\Delta ot}$ compared to the miR21$^{f/f}$ mice (Fig. 7f).

Despite the small changes in cancellous bone cell activity, μCT analysis detected significant alterations in cancellous bone architecture. In females, μCT of the vertebra revealed a slight increase in Tb.th (trabecular thickness) (Fig. 7g). On the other hand, in males μCT analysis detected significant increases in almost all the vertebral cancellous architecture parameters examined, including BV/TV (bone volume/tissue volume), Tb.Th, Tb.N (trabecular number), and material density miR21$^{\Delta ot}$ compared to miR21$^{f/f}$ mice (Fig. 7h). Similar alterations in cancellous architecture of the distal femur were also detected in female and male miR21$^{\Delta ot}$ compared to miR21$^{f/f}$ mice (Fig. 8).

Sex-divergent miR21 regulation of osteocyte cytokine production and release differentially controls osteoclastogenesis.

Consistent with the *in vivo* decreases in osteoclast number and surface in the miR21$^{\Delta ot}$ compared to miR21$^{f/f}$ female mice, less mature osteoclasts were generated *in vitro* from female miR21$^{\Delta ot}$ compared to miR21$^{f/f}$ non-adherent BMCs (Fig. 9a). On the other hand, *in vitro* generation of mature osteoclasts from male miR21$^{\Delta ot}$ and miR21$^{f/f}$ non-adherent BMCs did not differ (Fig. 9b).

To further examine the mechanisms underlying the sex-specific osteoclast effects of osteocytic miR21 removal, we generated osteoclasts from wildtype BMCs cultured with CM from osteocyte-enriched miR21$^{\Delta ot}$ and miR21$^{f/f}$ bone cultures, as illustrated in Fig. 9c. Consistent with our *in vivo* results, addition of 50% CM from miR21$^{\Delta ot}$ females led to 0.7-fold less mature osteoclasts (Fig. 9d), while addition of only 25% CM was not sufficient to reduce osteoclast number or gene expression (Fig. 10a). Conversely, addition of 50% CM from miR21$^{\Delta ot}$ males led to 3.8-fold more osteoclasts that were larger in size (Fig 9e), and addition of 25% CM led to a tendency towards increase in osteoclast number and significantly increased osteoclast gene expression (Fig. 10b).

Next, we investigated the effects of osteocytic miR21 deficiency on osteocyte cytokine production and release. Consistent with the sex-dimorphic effects on osteoclastogenesis, mRNA levels of several pro-osteoclastogenic cytokines, IL-6, MCP-1, M-CSF, and VEGF-A were reduced in bone lysates from female, but not male miR21$^{\Delta ot}$ compared to miR21$^{f/f}$ mice (Fig. 9f,g). Further, osteocytic-miR21 deletion induced sex-specific inflammatory cytokine protein alterations in CM from marrow-flushed osteocyte-enriched bone. In CM from miR21$^{\Delta ot}$ female bones, M-CSF and VEGF protein levels showed tendencies towards decrease, whereas, in CM from miR21$^{\Delta ot}$ male bones, M-CSF and VEGF protein levels were increased, although MCP-1 levels were decreased (Fig. 9h,I). Interestingly, in serum from these mice, an opposite pattern of expression was observed for several inflammatory

cytokines altered in CM from miR21$^{\Delta ot}$ bones (Tables 1,2). These pieces of evidence suggest that removal of osteocytic miR21 alters osteoclastogenesis by modifying osteocyte-derived inflammatory cytokine production and release in the local bone microenvironment, as illustrated in Fig. 9j.

In addition, we detected sex-dependent decreases in the mRNA levels of several cytokines known to inhibit osteoblast differentiation and activity. Specifically, in bone lysates from miR21$^{\Delta ot}$ females, only SOST mRNA levels were reduced (Fig. 11a). On the other hand, in miR21$^{\Delta ot}$ male bones, IL-1β, DKK1, and SOST mRNA expression was significantly decreased compared to miR21$^{f/f}$ mice (Fig. 11b).

Moreover, consistent with the sex-divergent effects of osteocytic-miR21 deletion on osteocyte cytokine production, sex-specific changes in several signaling pathways previously shown to be involved in regulating cytokine production and secretion were detected by Milliplex cell-signaling array analysis in bone lysates (Fig. 12a and Tables 3,4). Specifically, decreases in phosphorylated/total levels of ERK1/2 (−38%), STAT3 (−26%) and p38 (−28%) were detected in miR21$^{\Delta ot}$ females, but not in males. Moreover, miR21$^{\Delta ot}$ females exhibited a tendency towards increased phosphorylated/total NF-κB (+23%) levels. Further, while miR21$^{\Delta ot}$ males exhibited increased phosphorylated/total p70S6K (+22%) levels, females exhibited a tendency towards decreased p70S6K (−15%) levels. On the other hand, osteocytic miR21 deficiency induced similar decreases in JNK signaling in both females (−35%) and males (−28%), although significance was only reached in female mice.

miR21 has sex-independent effects on bone mechanical properties.

Despite the sex-specific effects of osteocytic miR21 deficiency on bone cell activity and architecture, femoral bone mechanical properties were significantly higher in both female and male miR21$^{\Delta Ot}$ mice compared to the respective miR21$^{f/f}$ controls. In particular, in females, femur mechanical testing by 3-point bending detected significantly higher post-yield and total displacement (+35% and +29%), post-yield and total work (+19% and +17%), as well as the post-yield material property total strain (+26%), in miR21$^{\Delta ot}$ compared to miR21$^{f/f}$ mice (Table 5). No changes in the pre-yield mechanical properties at either the structural or material levels were detected in the female mice. In males, even greater increases were detected in post-yield and total displacement (+94% and +60%), post-yield and total work (+71% and +56%), as well as the post-yield material properties, total strain and toughness (+56% and +28%) in miR21$^{\Delta ot}$ compared to miR21$^{f/f}$ mice (Table 6). On the other hand, decreases in the pre-yield structural property, displacement to yield, and the pre-yield material property, yield stress, were detected in the male miR21$^{\Delta ot}$ compared to miR21$^{f/f}$ mice. Taken together, these findings suggest that bones from miR21$^{\Delta ot}$ mice are more ductile, providing a potential mechanical advantage since the bones are more tolerant to damage accrual and, thus, less brittle and less susceptible to fracture. Given differences exist both at the structural and material level, it suggests that fundamental differences in the properties of the matrix underlie the enhanced mechanical properties.

Discussion

There is growing evidence that osteocytes are key regulators of bone homeostasis and orchestrators of bone cell activity [1]. In previous studies, we showed that miR21 expression is low in the absence of osteocytic Cx43 and in old female mice, and low miR21 levels are responsible for the increase in osteocyte apoptosis in the Cx43-deficient cells [15]. Additionally, we demonstrated that osteocyte apoptosis directly promotes osteocyte cytokine production and stimulates osteoclast differentiation.

Here we offer additional insights into the role of miR21 in osteocytes. We now provide evidence that the miR21 locus exerts a sex-divergent role in osteocytes regulating bone mass/geometry through paracrine actions on osteoblasts and osteoclasts. Further, we reveal a potential mechanism by which miR21 removal from osteocytes differentially alters bone turnover by sex-specific regulation of key signaling pathways in osteocytes as well as cytokine production/secretion. Similar sex-divergent effects have been found in mice expressing a Cx43 mutant lacking the C-terminus domain [19,20]. Thus, female mice expressing the truncated Cx43 molecule exhibit decreased cancellous bone mass, but intact cortical bone [19], whereas males exhibit no change in cancellous bone but periosteal expansion, reduced thickness and increased porosity in cortical bone [20]. Interesting, we also demonstrate that despite the sex-divergent effects on osteocyte viability and bone turnover, osteocytic miR21 negatively influences bone mechanical properties in a sex-independent manner.

Our studies also revealed a site specific consequence of osteocytic miR21 deletion, with different results when analyses were performed in cortical versus cancellous bone. Based on previous evidence that the DMP1-8kb-Cre transgene is expressed in both appendicular and axial skeleton [19,21-24], and on the fact that miR21 deletion alters bone cells and bone structure in both compartments, our data suggest that that the different effect of miR21 deletion is due to intrinsic differences in the bones rather than differential miR21 expression. Nevertheless, future studies will be carried out to established the basis for the diverse consequences of osteocytic miR21 deletion.

In the current study, we demonstrate that miR21 deficiency reduces osteocyte viability and alters mitochondria gene expression in female mice. Consistent with this, *in vitro* inhibition of miR21 expression by transfecting a miR21 antagomir increases cell death in MLO-Y4 osteocytic cells [15]. Further, adenovirus-Cre infection of miR21$^{f/f}$ calvaria bones leads to morphological changes in osteocytes consistent with apoptosis, as well as an increase in the expression of the apoptosis-associated genes, also reported here. These anti-apoptotic effects of miR21 are consistent with numerous studies showing that miR21 promotes cell survival by directly targeting and inhibiting FasL and PTEN [25-27]. In particular, we previously demonstrated that increases in osteocyte apoptosis in Cx43-deficient osteocytic cells and bones from old female mice, are due to low miR21 levels which increase PTEN levels and consequently reduce Akt signaling [15]. In cardiac tissue, miR21 has been shown to directly promote mitochondrial cytochrome B translation and reduce reactive oxygen species (ROS) production [28]. Additionally, miR21 promotes mitochondrial homeostasis and adaptation in mTORc1-activated cells [29]. Further, miR21 promotes cancer cell-survival by down-

regulating PTEN and consequently activating the PI3K/AKT/mTOR pathway [30]. We also detected sex-dependent alterations in phosphorylated levels of the mTOR substrate, p70S6K, with higher p70S6K levels in males and trends towards lower Akt and p70S6K levels in female miR21$^{\Delta ot}$ mice. Interestingly, consistent with our findings in miR21$^{\Delta ot}$ males, several other studies have found that inhibition of miR21 protects against fibrosis by improving mitochondrial function [31,32]. Taken together these pieces of evidence highlight the possibility that miR21 regulation of mTORc1 signaling in osteocytes may underlie these sex-divergent effects on osteocyte viability and mitochondrial function, however, additional studies are needed to clearly elucidate these mechanisms.

miRs in general, and miR21 in particular, target a large number of genes, in a cell context-dependent manner. Indeed, some of the genes included in our studies have already been shown to be targeted by miR21 regulation. Examples are the apoptosis- and mitochondria-associated genes. It is not clear, however, whether the effects of miR21 on gene regulation are a direct consequence of altered transcription or an indirect regulation of expression downstream of other genes or even of intracellular kinases. Nevertheless, our findings highlight a novel sex-divergent role of miR21 in osteocytes and raise the possibility that similar sex-divergent miR21 regulation exists in other tissues.

Further, consistent with the effects of osteocytic miR21 removal on osteocyte viability, RANKL/OPG mRNA levels were only increased in bones from miR21$^{\Delta ot}$ females. Surprisingly, despite the RANKL/OPG ratio changes osteoclast differentiation and resorption were attenuated in miR21$^{\Delta ot}$ females, but elevated in miR21$^{\Delta ot}$ males. Similar to our findings in miR21$^{\Delta ot}$ females, Hu et. al, found that osteoclast function was inhibited in global miR21 deficient (miR21$^{-/-}$) mice in spite of the fact that RANKL production and secretion were increased [33]. However, since mice were not separated by sex and because miR21, which is known to regulate osteoclast differentiation and survival [26,34], was globally deleted, it is unclear if the inhibitory effects on osteoclasts in this study were due to a lack of miR21 regulation in osteocytes or a direct result of miR21 deficiency in osteoclasts. In our study, we found that addition of osteocyte-enriched bone culture CM from miR21$^{\Delta ot}$ females suppressed osteoclasts, whereas CM from miR21$^{\Delta ot}$ males stimulated osteoclasts, suggesting that these effects are due to the lack of miR21 in osteocytes. Furthermore, the fact that these results occurred independently of whether female or male BMCs were used, suggests that the sex-specific effects of osteocytic miR21 removal on osteoclasts are due to miR21 regulation in osteocytes rather than direct effects on osteoclasts.

In addition, miR21 regulation in osteoblasts has been shown to promote differentiation and mineralization [35]. Consistent with this, osteoblast differentiation and activity were altered in miR21$^{-/-}$ mice [33]. When cultured *ex vivo* osteogenic differentiation potential of miR21$^{-/-}$ BMCs was decreased, while colony forming efficiency and proliferation rates were increased. Interestingly, despite these changes, osteoblast number and activity were unaltered *in vivo*, possibly because mice of both sexes were combined in the *in vivo* study. We now report that osteocytic miR21 deletion also altered osteoblast number and activity in a sex- and site-dependent manner. Further, consistent with the effects on bone cell differentiation and activity, osteocytic miR21 deficiency induced sex- and compartment-

specific effects on bone mass and architecture. Future studies will be performed to determine whether the mild effect of miR21 deletion on bone mass and architecture is exacerbated with aging.

Based on the non-cell autonomous effects on osteoclasts and osteoblasts detected in the miR21$^{\Delta ot}$ mice, we next investigated the effects of miR21 regulation on osteocyte cytokine production and release. Consistent with the sex-dimorphic effects on osteoclasts and osteoblasts we found that mRNA levels of several cytokines were reduced in bones from female, but not male miR21$^{\Delta ot}$ mice. On the other hand, we detected decreases in the mRNA levels of IL-1β and DKK1, which negatively regulate osteoblast differentiation and activity, in bones from miR21$^{\Delta ot}$ males, but not females. Further, in CM from miR21$^{\Delta ot}$ bones, M-CSF and VEGF protein levels were increased in males, but showed tendencies towards decrease in females. Additionally, given the changes in IL-6 expression detected at the mRNA level it is also possible that IL-6 levels are altered in the miR21$^{\Delta ot}$ CM, however because the levels were greater than the standard use in the multiplex assays we were unable to measure them. Interestingly, we also found several cytokines exhibited an opposite pattern of expression in serum compared to CM from miR21$^{\Delta ot}$ bones, suggesting that that removal of osteocytic miR21 exerts non-cell autonomous effects on osteoclasts and osteoblasts by locally rather than systemically altering osteocyte-derived cytokine levels.

In addition, osteocytic miR21 deficiency altered osteocyte signaling pathways in a sex-dependent manner. Interestingly, several signaling pathways that are regulated by previously identified miR21 target genes were downregulated in miR21$^{\Delta ot}$ females, but not males, as illustrated in Fig. 12a. In particular, phosphorylated ERK1/2, p38, and STAT3 levels were significantly reduced, whereas, phosphorylated NF-κB levels showed tendencies towards increase in miR21$^{\Delta ot}$ female bones. Consistent with these findings, previous studies have shown that miR21 directly targets inhibitors of ERK1/2 (Spry1/2), p38 (SMAD7) and STAT3 (PIAS3) [35-37]. Additionally, miR21 targets PDCD4, which in turn activates NF-κB signaling [33,38]. Nevertheless, while these findings suggest that miR21 regulates osteocyte signaling pathways and cytokine production/secretion in sex-specific manner, additional studies are required to clearly elucidate the molecular events mediating these autocrine and paracrine effects of osteocytic miR21 on bone metabolism.

Alterations in miR21 expression have been detected in numerous diseases. However, the tissue-specific roles of miR21 under physiological and pathological conditions remains unclear. In some cases miR21 has been shown to promote disease progression, while in others miR21 is protective [39,40]. While there are several potential explanations for the varying results regarding the role of miR21 in different tissues under normal and disease conditions, given the findings of our present study, it is possible that the differential effects of miR21 are due to the sex-dependent roles of miR21. Consistent with this notion, work by Queirós et. al, detected sex differences in the expression of several miRs including miR21, as well as, miR24, miR27a, miR27b, miR106a and miR-106b that negatively regulate MAPK/ERK signaling in the heart [41]. Additionally, this study showed that estrogen modulates the expression of these miRs in a sex-specific manner via estrogen receptor (ER) β. Further, in bone, studies have shown that induction of miR21 during osteoclastogenesis preserves survival through negative regulation of FasL and estrogen stimulates osteoclast

apoptosis by antagonizing miR21 [26]. Indeed, given the increasing number of pharmaceutical companies working to develop miR-based drugs combined with the growing number of studies identifying gender-dependent adverse drug reactions [42], our findings highlight the importance of considering sex-dependent miR roles when developing therapeutics.

Interestingly, despite these sex-specific effects of osteocytic miR21 deficiency, both female and male miR21$^{\Delta Ot}$ mice exhibited markedly higher femoral cortical bone mechanical properties compared to the respective miR21$^{f/f}$ controls. In particular, our findings that osteocytic miR21 deficiency enhanced the femur post-yield mechanical properties, suggest that bones from miR21$^{\Delta ot}$ mice are more ductile, providing a potential mechanical advantage since the bones are more tolerant to damage accrual and, thus, less brittle and less susceptible to fracture. As improvements in mechanical properties cannot be accounted for by the alterations observed at the cellular and structural level, it is likely that they result from differences in the matrix itself. Traditionally, alterations in post-yield properties are due to collagen structure/cross-linking. In future studies, we will work to uncover the molecular and tissue-level mechanisms by which osteocytic miR21 negatively influences bone mechanical integrity.

Moreover, consistent with these negative sex-equivalent effects of miR21 on bone mechanical properties, several studies have found that miR21 levels are upregulated in serum, bone tissue, and bone cells (osteoblasts and osteoclasts) of osteoporotic patients compared to controls [43]. Additionally, miR21 levels were strongly inversely correlated with BMD and fracture incidence in osteoporotic patients. Thus, our findings that removal of osteocytic miR21 enhances bone biomechanical properties in both sexes, suggest a therapeutic potential of miR21 antagomir treatment to prevent bone fragility in aging in females and males. Further, given the fact that altered miR21 expression is most commonly seen under pathological conditions, our results provide a basis for future studies to test whether osteocytic miR21 deficiency protects against bone loss induced by sex-steroid deficiency, unloading, or aging.

Collectively, our findings provide evidence that the miR21 locus exerts both sex-divergent and sex-equivalent roles in osteocytes. miR21 directly regulates cell viability/mitochondrial function in osteocytes and subsequently alters bone metabolism and architecture through paracrine actions on osteoblasts and osteoclasts in a different manner in males and females. However, despite these sex-dependent effects, removal of osteocytic miR21 enhances bone mechanical properties in both sexes. Overall, our findings provide novel insights into the sex-dependent and -independent mechanisms by which miR21 regulation in osteocytes alters bone (Fig. 12b), which offer a basis for future studies that could eventually lead to new therapeutic targets to treat bone fragility.

Materials and Methods

Mice

miR21 floxed mouse strain was engineered with lox cassettes on both sides of the mmu-miR-21 genomic locus (named miR21$^{f/f}$) [15], and crossed with DMP1-8kb-Cre mice [44]

to obtain female and male miR21$^{f/f}$ and miR21$^{f/f}$;DMP1-8kb-Cre (miR21$^{\Delta ot}$) mice. All mice were of the C57BL/6 background, fed a regular diet and water *ad libitum* and maintained on a 12h light/dark cycle. The protocols involving mice were approved by the Institutional Animal Care and Use Committee of Indiana University School of Medicine.

RNA extraction and qRT-PCR

Total RNA was isolated using TRIzol (Invitrogen, Grand Island, NY) [45]. Reverse transcription was performed using a high-capacity cDNA kit (Applied Biosystems, Foster City, CA). qPCR was performed using the Gene Expression Assay Mix TaqMan Universal Master Mix with an ABI 7900HT real-time PCR system. Gene expression was corrected by the levels of the house-keeping gene glyceraldehyde 3-phosphate dehydrogenase (GAPDH). Primers and probes were commercially available (Applied Biosystems, Foster City, CA) or were designed using the Assay Design Center (Roche Applied Science, Indianapolis, IN). Expression levels of miR21 (assay ID:000397) and the housekeeping miR135 (assay ID:001230) were evaluated as published [15]. Relative expression was calculated using the ΔCt method.

Body weight and bone mineral density (BMD) by dual energy x-ray absorptiometry (DXA)

BMD was measured monthly from 1 to 4 months of age by DXA/PIXImus (G.E. Medical Systems, Lunar Division, Madison, WI) [45]. Body weight was measured at the time of the DXA scan. BMD measurements included total (whole body excluding the head and tail), femoral (entire femur) and spinal (L1-L6 lumbar vertebrae) BMD. Calibration was performed using a standard control phantom before scanning, as recommended by the manufacturer.

μCT analysis

Femur and L4 vertebra were harvested from 4-month-old mice. Female bones were scanned using the Scanco μCT-35 system (Scanco Medical AG, Brüttisellen, Switzerland) using a 50kV source, 120 mA, 151 milliseconds integration time, and 10μm voxel resolution [45]. Male bones were scanned using a 65kV source, 0.5mm Al filter, 0.7 degree rotation and two-image averaging with an isotropic voxel size of 9μm using a SkyScan 1176 system (SkyScan, Kontich, Belgium) [46]. Two different systems were used due to constrained instrument availability. The terminology and units used for μCT are those recommended by the American Society for Bone and Mineral Research (ASBMR) [47].

Bone histomorphometry

Femur and vertebra from 4-month-old mice were fixed in 10% neutral buffered formalin and embedded using previously established methods at the ICMH Histology and Histomorphometry Core [46]. To allow for dynamic histomorphometry mice were injected intraperitoneally with calcein (20 mg/kg; Sigma) and alizarin red (20 mg/kg; Sigma) 7 and 2 days prior to sacrifice, respectively. Dynamic histomorphometry was performed on unstained methyl methacrylate-embedded L1-L3 vertebra (sagittal) and femur mid-diaphysis (transverse) sections using an epifluorescence microscope. Osteoclasts were quantified in TRAPase/Toluidine blue stained femur mid-diaphysis and vertebra sections and osteoblasts

in von Kossa/McNeal stained-sections. Histomorphometric analysis was performed using OsteoMeasure high resolution digital video system (OsteoMetrics Inc., Decatur, GA, USA). The terminology and units used are those recommended by the ASBMR Histomorphometry Nomenclature Committee [48].

Biomechanical testing

Three-point bending testing of the femoral mid-diaphysis was performed as published, using a servo-hydraulic test system (TestResources Inc., Shakopee, MN, USA) [19,46]. Femora were loaded until failure in an anterior–posterior direction with the upper contact area at the mid-diaphysis (50% total bone length) and the bottom contact points centered around this point and separated by 8mm. Cross-sectional moment of inertia and anterior–posterior diameter were determined by μCT and were used to calculate material-level properties [19].

Ex vivo bone organ cultures

Long bones were isolated from 2-month-old miR21$^{f/f}$ and miR21$^{\Delta ot}$ mice. Bone-marrow cells (BMCs) were flushed out with α- MEM and osteocyte-enriched long bones were cultured *ex vivo* in 10% FBS and 1% penicillin/streptomycin (P/S)-α-MEM supplemented for 48h. Conditioned media was collected and stored at −20°C until used for the osteoclastogenesis assays and cytokine arrays.

Osteoclast assays

BMCs were isolated from C57BL/6 mice by flushing the bone marrow out with 10% FBS and 1% P/S-α-MEM and cultured for 48h [15,45]. Next, non-adherent cells were collected and 2×10^4cells/cm^2 were seeded on 96-well plates and cultured with conditioned media collected from *ex vivo* cultures of osteocyte-enriched marrow-flushed long bones from miR21$^{f/f}$ and miR21$^{\Delta ot}$ mice. Additionally, BMCs isolated from the miR-21$^{f/f}$ and miR21$^{\Delta ot}$ mice were cultured in 10% FBS and 1% P/S-α-MEM for 48h. Next, non-adherent cells were collected and 2×10^4cells/cm^2 were seeded on 96-well plates. RANKL (80ng/ml) and M-CSF (20ng/ml) were added to induce osteoclast differentiation and media was changed every 3 days for 7 days. Cells were stained using a TRAPase kit (Sigma-Aldrich) and mature osteoclasts exhibiting 3 or more nuclei were quantified. Images were acquired using a Zeiss Axiovert 35 microscope equipped with a digital camera. Osteoclast size and number of nuclei were quantified using ImageJ.

Multiplex cytokine and cell-signaling assays

Cytokines in serum and conditioned media from osteocyte-enriched *ex vivo* bone organ cultures of miR21$^{f/f}$ and miR21$^{\Delta ot}$ mice, were measured using the Bioplex protein array system at the Multiplex analysis core at IUSM. For the cytokine assay, premixed magnetic beads of the Milliplex mouse cytokine/chemokine 32 plex kit was used (Milliplex, Burlington, MA). Cell-signaling pathway alterations induced by deletion of osteocytic miR21 were examined in miR21$^{f/f}$ and miR21$^{\Delta ot}$ calvaria bone lysates. For the cell-signaling assays, premixed magnetic beads of the Milliplex multi-pathway 9-plex phospho- and total protein kits were used.

Cell culture and lentiviral transfection

miR21-silenced MLO-Y4 osteocytic cells were generated using short hairpin (sh)RNA Lentiviral Particles (Sigma-Aldrich Chemical Co., St. Louis, MO, USA), as previously reported,[5,44] and cultured as previously described. MLO-Y4 osteocytic cells silenced or not for Cx43 were plated at the density of 2×10^4 cells/cm^{-2} on 48-well plates coated with type I rat tail collagen and cultured overnight. Cells were transiently transfected using Lipofectamine RNAiMAX reagent (Invitrogen) containing miRIDIAN negative control inhibitor, miR21 inhibitor, negative control mimic, or miR21 mimic (GE Healthcare Bio-Sciences, Pittsburgh, PA, USA) at a final concentration of 0.1 nM in medium without serum and penicillin/ streptomycin for 6 h. Next, 2x concentrated medium was added to each well and then cultured overnight. Medium was changed to a regular growing medium, and cells were then cultured for an additional 24 h before isolating mRNA. miR21 levels were decreased by 60% in MLO-Y4 scramble cells and by 91% in MLO-Y4 Cx43 shRNA cells treated with miR21 inhibitor, as measured by qPCR. miR21 levels were increased by 44% in MLO-Y4 scramble cells and 234% in MLO-Y4 Cx43 shRNA cells treated with the miR21 mimic.

Whole-mount skeletal staining

Cartilage and mineralized tissue were analyzed in 6-day old newborn mice using alizarin red/alcian blue staining, as previously published [49].

Circulating metabolites

Blood was collected by cheek bleeding after 6 hours of fasting. Plasma was separated, aliquoted, and stored at −80 °C until used. Plasma N-terminal propeptide of type I procollagen (P1NP) (Immunodiagnostic Systems Inc., Fountain Hill, AZ, USA, cat.#AC-33F1) and C-telopeptide fragments (CTX) (cat.#AC-06F1) were measured as described by the manufacturer. Alkaline phosphatase (ALP) activity was assessed by a standard automated method using a Randox Daytona chemical analyzer (Northern Ireland, United Kingdom).

Statistical analysis

Data were analyzed using SigmaPlot (Systat Software Inc., San Jose, CA). Data are reported as mean ± SD. Data were evaluated by Student’s t-test or two-way ANOVA and differences with $p<0.05$ were considered statistically significant.

Acknowledgements

This research was supported by the National Institutes of Health R01-AR067210 to LIP and R01-CA155332 to MI. HMD is supported by the Cagiantas-fellowship at Indiana University School of Medicine. MWA is supported by an NIH F30-DK115162 fellowship. RPC received a scholarship from Coordination of Improvement of Higher Level Personnel (CAPES), Brazil (PDE# 232636/2014-1). EGA is supported by an NIH T32-AR065971 grant, JED by a Ruth L. Kirschstein NRSA Short-Term Institutional Research Training Grant (NRSA) through the NIH (#4T35HL 110854-05). We thank Dr. Wallace for the insightful discussion over the mechanical effects of osteocytic miR21 deletion and the ICMH Histology and Histomorphometry Core for bone tissue section preparation and staining. Cell-signaling and cytokine array analysis and data interpretation was performed with the support of the Multiplex Analysis Core at Indiana University Melvin and Bren Simon Cancer Center, partially funded by the National Institutes of Health UL1TR002529 NCATS Clinical and Translational Sciences Award to Indiana Clinical and

Translational Sciences Institute (CTSI). The content is solely the responsibility of the authors and does not necessarily represent the official views of the National Institutes of Health.

Abbreviations:

miR	microRNA
miR21$^{\Delta ot}$	miR21$^{f/f}$
DMP1	8kb-Cre
GADH	glyceraldehyde 3-phosphate dehydrogenase
DXA	dual-energy X-ray absorptiometry
BMD	bone mineral density
ASBMR	American Society for Bone and Mineral Research
BMCs	bone marrow cells
P/S	penicillin/streptomycin
FBS	fetal bovine serum
RANKL	receptor activator of nuclear factor κ ligand, M-CSF, macrophage-colony stimulating factor
TRAPase	tartrate-resistant acid phosphatase
sh	short hairpin
qPCR	quantitative polymerase chain reaction
P1NP	N-terminal propeptide of type I procollagen
ALP	alkaline phosphatase
VMP1	vacuole membrane protein-1
MS/BS	mineralized surface per total bone surface
BFR/BS	bone formation rate per bone surface
MAR	mineral apposition rate
N.Oc/BS	osteoclast number per bone surface
Oc.S/BS	osteoclast surface per bone surface
N.Ob/BS	osteoblast number per bone surface
Ob.S/BS	osteoblast surface per bone surface
TA	tissue area
BA	bone area

C.Th	cortical thickness
μCT	microcomputed tomography
BV/TV	bone volume/tissue volume
Tb.th	trabecular thickness
Tb.N	trabecular number
CM	conditioned media
ROS	reactive oxygen species

References

1. Bonewald LF. The Amazing Osteocyte. J Bone Miner Res. 2011; 2: 229–238.
2. Jilka RL, Weinstein RS, Bellido T, Roberson P, Parfitt AM, Manolagas SC. Increased bone formation by prevention of osteoblast apoptosis with parathyroid hormone. J Clin Invest. 1999; 4: 439–446.
3. Plotkin LI, Weinstein RS, Parfitt AM, Roberson PK, Manolagas SC, Bellido T. Prevention of osteocyte and osteoblast apoptosis by bisphosphonates and calcitonin. J Clin Invest. 1999; 10: 1363–1374.
4. Kousteni S, Bellido T, Plotkin LI, O'Brien CA, Bodenner DL, Han L, Han K, Di Gregorio GB, Katzenellenbogen JA, Katzenellenbogen BS, Roberson PK, Weinstein RS, Jilka RL, Manolagas SC. Nongenotropic, sex-nonspecific signaling through the estrogen or androgen receptors: dissociation from transcriptional activity. Cell. 2001; 5: 719–730.
5. Plotkin LI, Lezcano V, Thostenson J, Weinstein RS, Manolagas SC, Bellido T. Connexin 43 is required for the anti-apoptotic effect of bisphosphonates on osteocytes and osteoblasts in vivo. J Bone Miner Res. 2008; 11: 1712–1721.
6. Plotkin LI, Bellido T. Osteocytic signalling pathways as therapeutic targets for bone fragility. Nat Rev Endocrinol. 2016; 10: 593–605.
7. Tomkinson A, Reeve J, Shaw RW, Noble BS. The death of osteocytes via apoptosis accompanies estrogen withdrawal in human bone. J Clin Endocrinol Metab. 1997; 9: 3128–3135.
8. Weinstein RS, Jilka RL, Parfitt AM, Manolagas SC. Inhibition of osteoblastogenesis and promotion of apoptosis of osteoblasts and osteocytes by glucocorticoids: potential mechanisms of their deleterious effects on bone. J Clin Invest. 1998; 2: 274–282.
9. Aguirre JI, Plotkin LI, Stewart SA, Weinstein RS, Parfitt AM, Manolagas SC, Bellido T. Osteocyte apoptosis is induced by weightlessness in mice and precedes osteoclast recruitment and bone loss. J Bone Min Res. 2006; 4: 605–615.
10. Qiu S, Rao DS, Palnitkar S, Parfitt AM. Age and distance from the surface but not menopause reduce osteocyte density in human cancellous bone. Bone. 2002; 2: 313–318.
11. Almeida M, Han L, Martin-Millan M, Plotkin LI, Stewart SA, Roberson PK, Kousteni S, O'Brien CA, Bellido T, Parfitt AM, Weinstein RS, Jilka RL, Manolagas SC. Skeletal involution by age-associated oxidative stress and its acceleration by loss of sex steroids. J Biol Chem. 2007; 37: 27285–27297.
12. He X, Eberhart JK, Postlethwait JH. MicroRNAs and micromanaging the skeleton in disease, development and evolution. J Cell Mol Med. 2009; 4: 606–618.
13. Smith-Vikos T, Slack FJ. MicroRNAs and their roles in aging. J Cell Sci. 2012; Pt 1: 7–17.
14. Taipaleenmaki H, Bjerre L, Chen L, Kauppinen S, Kassem M. MicroRNAs: Targets for enhancing osteoblast differentiation and bone formation. Eur J Endocrinol. 2011.
15. Davis HM, Pacheco-Costa R, Atkinson EG, Brun LR, Gortazar AR, Harris J, Hiasa M, Bolarinwa SA, Yoneda T, Ivan M, Bruzzaniti A, Bellido T, Plotkin LI. Disruption of the Cx43/miR21

pathway leads to osteocyte apoptosis and increased osteoclastogenesis with aging. Aging Cell. 2017; 3: 551–563.

16. Garzon R, Calin GA, Croce CM. MicroRNAs in Cancer. Annu Rev Med. 2009; 167–179. [PubMed: 19630570]
17. Plotkin LI. Apoptotic osteocytes and the control of targeted bone resorption. Curr Osteoporos Rep. 2014; 1: 121–126.
18. Kalajzic I, Matthews BG, Torreggiani E, Harris MA, Divieti PP, Harris SE. In vitro and in vivo approaches to study osteocyte biology. Bone. 2013; 2: 296–306.
19. Pacheco-Costa R, Davis HM, Sorenson C, Hon MC, Hassan I, Reginato RD, Allen MR, Bellido T, Plotkin LI. Defective cancellous bone structure and abnormal response to PTH in cortical bone of mice lacking Cx43 cytoplasmic C-terminus domain. Bone. 2015; 632–643. [PubMed: 26409319]
20. Moorer MC, Hebert C, Tomlinson RE, Iyer SR, Chason M, Stains JP. Defective signaling, osteoblastogenesis, and bone remodeling in a mouse model of connexin43 C-terminal truncation. J Cell Sci. 2017; 3: 531–540.
21. Bivi N, Nelson M, Lee R, Benson JD, Condon K, Li J, Allen MR, Bellido T, Plotkin LI. Cx43 in osteocytes, but not in osteoblasts, is required to preserve osteocyte viability, bone geometry and material stiffness. J Bone Miner Res. 2010; Suppl 1: S112.
22. Bivi N, Nelson MT, Faillace ME, Li J, Miller LM, Plotkin LI. Deletion of Cx43 from osteocytes results in defective bone material properties but does not decrease extrinsic strength in cortical bone. Calcif Tissue Int. 2012; 3: 215–224.
23. Tu X, Delgado-Calle J, Condon KW, Maycas M, Zhang H, Carlesso N, Taketo MM, Burr DB, Plotkin LI, Bellido T. Osteocytes mediate the anabolic actions of canonical Wnt/b-catenin signaling in bone. Proc Natl Acad Sci U S A. 2015; 5: E478–E486.
24. Hammond MA, Berman AG, Pacheco-Costa R, Davis HM, Plotkin LI, Wallace JM. Removing or truncating connexin 43 in murine osteocytes alters cortical geometry, nanoscale morphology, and tissue mechanics in the tibia. Bone. 2016; 85–91.
25. Francis H, McDaniel K, Han Y, Liu X, Kennedy L, Yang F, McCarra J, Zhou T, Glaser S, Venter J, Huang L, Levine P, Lai JM, Liu CG, Alpini G, Meng F. Regulation of the extrinsic apoptotic pathway by microRNA-21 in alcoholic liver injury. J Biol Chem. 2014.
26. Sugatani T, Hruska KA. Down-regulation of miR-21 biogenesis by estrogen action contributes to osteoclastic apoptosis. J Cell Biochem. 2013; 6: 1217–1222.
27. Ma X, Conklin DJ, Li F, Dai Z, Hua X, Li Y, Xu-Monette ZY, Young KH, Xiong W, Wysoczynski M, Sithu SD, Srivastava S, Bhatnagar A, Li Y. The oncogenic microRNA miR-21 promotes regulated necrosis in mice. Nat Commun. 2015; 7151. [PubMed: 25990308]
28. Li H, Zhang X, Wang F, Zhou L, Yin Z, Fan J, Nie X, Wang P, Fu XD, Chen C, Wang DW. MicroRNA-21 Lowers Blood Pressure in Spontaneous Hypertensive Rats by Upregulating Mitochondrial Translation. Circulation. 2016; 10: 734–751.
29. Lam HC, Liu HJ, Baglini CV, Filippakis H, Alesi N, Nijmeh J, Du H, Lope AL, Cottrill KA, Handen A, Asara JM, Kwiatkowski DJ, Ben-Sahra I, Oldham WM, Chan SY, Henske EP. Rapamycin-induced miR-21 promotes mitochondrial homeostasis and adaptation in mTORC1 activated cells. Oncotarget. 2017; 39: 64714–64727.
30. Go H, Jang JY, Kim PJ, Kim YG, Nam SJ, Paik JH, Kim TM, Heo DS, Kim CW, Jeon YK. MicroRNA-21 plays an oncogenic role by targeting FOXO1 and activating the PI3K/AKT pathway in diffuse large B-cell lymphoma. Oncotarget. 2015; 17: 15035–15049.
31. Gomez IG, MacKenna DA, Johnson BG, Kaimal V, Roach AM, Ren S, Nakagawa N, Xin C, Newitt R, Pandya S, Xia TH, Liu X, Borza DB, Grafals M, Shankland SJ, Himmelfarb J, Portilla D, Liu S, Chau BN, Duffield JS. Anti-microRNA-21 oligonucleotides prevent Alport nephropathy progression by stimulating metabolic pathways. J Clin Invest. 2015; 1: 141–156.
32. Chau BN, Xin C, Hartner J, Ren S, Castano AP, Linn G, Li J, Tran PT, Kaimal V, Huang X, Chang AN, Li S, Kalra A, Grafals M, Portilla D, MacKenna DA, Orkin SH, Duffield JS. MicroRNA-21 Promotes Fibrosis of the Kidney by Silencing Metabolic Pathways. Sci Transl Med. 2012; 121: 121ra118.
33. Hu CH, Sui BD, Du FY, Shuai Y, Zheng CX, Zhao P, Yu XR, Jin Y. miR-21 deficiency inhibits osteoclast function and prevents bone loss in mice. Sci Rep. 2017; 43191. [PubMed: 28240263]

34. Pitari MR, Rossi M, Amodio N, Botta C, Morelli E, Federico C, Gulla A, Caracciolo D, Di Martino MT, Arbitrio M, Giordano A, Tagliaferri P, Tassone P. Inhibition of miR-21 restores RANKL/OPG ratio in multiple myeloma-derived bone marrow stromal cells and impairs the resorbing activity of mature osteoclasts. Oncotarget. 2015; 29: 27343–27358.
35. Li H, Yang F, Wang Z, Fu Q, Liang A. MicroRNA-21 promotes osteogenic differentiation by targeting small mothers against decapentaplegic 7. Mol Med Rep. 2015; 1: 1561–1567.
36. Liu LZ, Li C, Chen Q, Jing Y, Carpenter R, Jiang Y, Kung HF, Lai L, Jiang BH. MiR-21 induced angiogenesis through AKT and ERK activation and HIF-1alpha expression. PLoS One. 2011; 4: e19139.
37. Ma X, Kumar M, Choudhury SN, Becker Buscaglia LE, Barker JR, Kanakamedala K, Liu MF, Li Y. Loss of the miR-21 allele elevates the expression of its target genes and reduces tumorigenesis. Proc Natl Acad Sci U S A. 2011; 25: 10144–10149.
38. Merline R, Moreth K, Beckmann J, Nastase MV, Zeng-Brouwers J, Tralhao JG, Lemarchand P, Pfeilschifter J, Schaefer RM, Iozzo RV, Schaefer L. Signaling by the Matrix Proteoglycan Decorin Controls Inflammation and Cancer Through PDCD4 and MicroRNA-21. Sci Signal. 2011; 199: ra75.
39. Rodrigues PM, Afonso MB, Simao AL, Carvalho CC, Trindade A, Duarte A, Borralho PM, Machado MV, Cortez-Pinto H, Rodrigues CM, Castro RE. miR-21 ablation and obeticholic acid ameliorate nonalcoholic steatohepatitis in mice. Cell Death Dis. 2017; 5: e2825.
40. Jia Z, Lian W, Shi H, Cao C, Han S, Wang K, Li M, Zhang X. Ischemic Postconditioning Protects Against Intestinal Ischemia/Reperfusion Injury via the HIF-1alpha/miR-21 Axis. Sci Rep. 2017; 1: 16190.
41. Queiros AM, Eschen C, Fliegner D, Kararigas G, Dworatzek E, Westphal C, Sanchez Ruderisch H, Regitz-Zagrosek V. Sex- and estrogen-dependent regulation of a miRNA network in the healthy and hypertrophied heart. Int J Cardiol. 2013; 5: 331–338.
42. Rademaker M Do women have more adverse drug reactions? Am J Clin Dermatol. 2001; 6: 349–351.
43. Seeliger C, Karpinski K, Haug AT, Vester H, Schmitt A, Bauer JS, van GM. Five Freely Circulating miRNAs and Bone Tissue miRNAs Are Associated With Osteoporotic Fractures. J Bone Miner Res. 2014; 8: 1718–1728.
44. Bivi N, Condon KW, Allen MR, Farlow N, Passeri G, Brun L, Rhee Y, Bellido T, Plotkin LI. Cell autonomous requirement of connexin 43 for osteocyte survival: consequences for endocortical resorption and periosteal bone formation. J Bone Min Res. 2012; 2: 374–389.
45. Pacheco-Costa R, Hassan I, Reginato RD, Davis HM, Bruzzaniti A, Allen MR, Plotkin LI. High Bone Mass in Mice Lacking Cx37 Due to Defective Osteoclast Differentiation. J Biol Chem. 2014; 12: 8508–8520.
46. Davis HM, Aref MW, Aguilar-Perez A, Pacheco-Costa R, Allen K, Valdez S, Herrera C, Atkinson EG, Mohammad A, Lopez D, Harris MA, Harris SE, Alen M, Bellido T, Plotkin LI. Cx43 overexpression in osteocytes prevents osteocyte apoptosis and preserves cortical bone quality in aging mice. JBMR Plus. 2018.
47. Bouxsein ML, Boyd SK, Christiansen BA, Guldberg RE, Jepsen KJ, Muller R. Guidelines for assessment of bone microstructure in rodents using micro-computed tomography. J Bone Miner Res. 2010; 7: 1468–1486.
48. Dempster DW, Compston JE, Drezner MK, Glorieux FH, Kanis JA, Malluche H, Meunier PJ, Ott SM, Recker RR, Parfitt AM. Standardized nomenclature, symbols, and units for bone histomorphometry: A 2012 update of the report of the ASBMR Histomorphometry Nomenclature Committee. J Bone Miner Res. 2013; 1: 2–17.
49. Tu X, Joeng KS, Nakayama KI, Nakayama K, Rajagopal J, Carroll TJ, McMahon AP, Long F. Noncanonical Wnt signaling through G protein-linked PKCdelta activation promotes bone formation. Dev Cell. 2007; 1: 113–127.

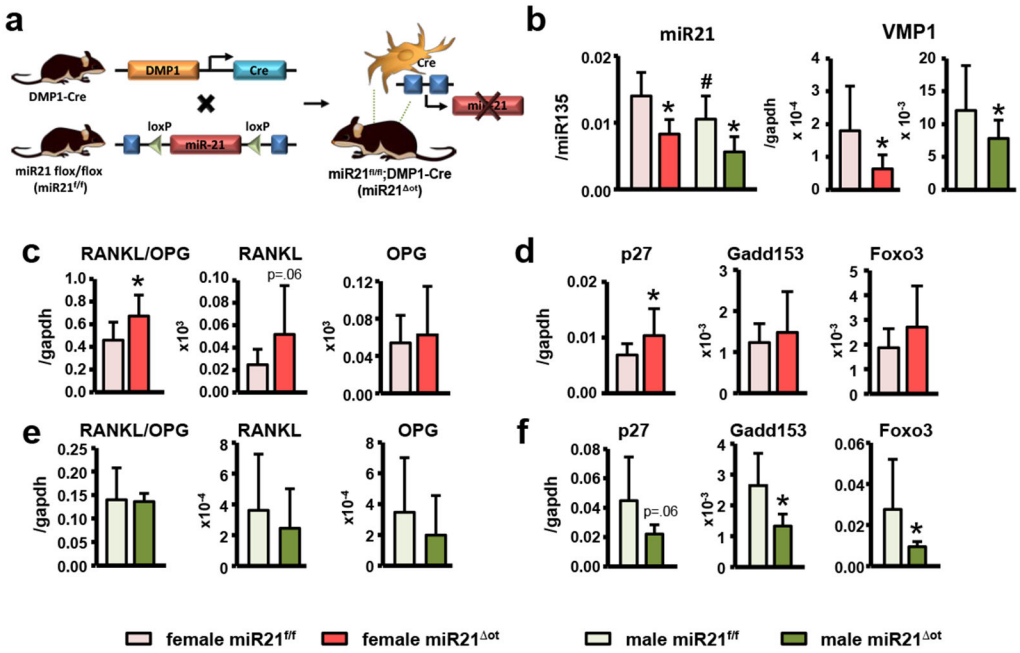

Figure 1. Sex-dependent miR21 regulation of osteocyte viability and mitochondrial function.

(a) Scheme illustrating generation of mouse model with osteocyte-targeted miR21 deletion. **(b)** miR-21 levels in calvaria bones from female and male miR21$^{f/f}$ and miR21$^{\Delta ot}$ mice by qPCR and corrected by miR135 (n= 10-14). mRNA levels of vacuole membrane protein-1 (VMP1) measured in calvaria bones from female and male miR21$^{fl/fl}$ and miR21$^{\Delta ot}$ mice. Bars represent mean ± s.d., *p<0.05 versus miR21$^{f/f}$ mice, $^{\#}$p<0.05 versus miR21$^{f/f}$ females, by two-way ANOVA (for miR21) or by t-test (for VMP1). **(c)** RANKL and OPG levels and **(d)** mRNA expression of apoptosis-associated genes measured in calvaria bones from female miR21$^{f/f}$ and miR21$^{\Delta ot}$ mice (n= 10-14). **(e)** RANKL and OPG levels and **(f)** mRNA expression of apoptosis-associated genes measured in calvaria bones from male miR21$^{f/f}$ and miR21$^{\Delta ot}$ mice (n= 10). Bars represent mean ± s.d., *p<0.05 versus miR21$^{f/f}$, by t-test.

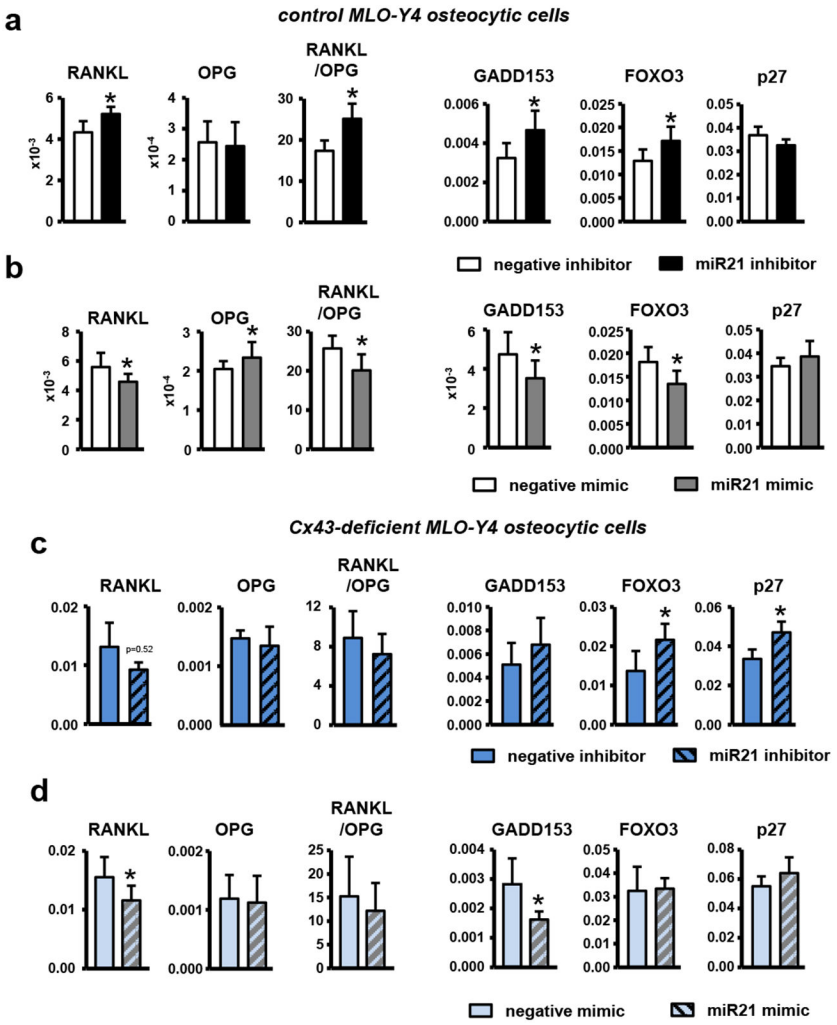

Figure 2. miR21 maintains osteocyte viability and regulates RANKL/OPG levels in control and Cx43-deficient MLO-Y4 osteocytic cells.

RANKL and OPG levels and apoptosis-associated gene expression (Gadd153, Foxo3, and P27) in miR-21 **(a)** antagomir and **(b)** mimic transfected MLO-Y4 osteoctyic cells, and in miR-21 **(c)** antagomir and **(d)** mimic transfected MLO-Y4 osteoctyic cells silenced for Cx43. Bars represent mean ± s.d., *p<0.05 versus negative control, by t-test.

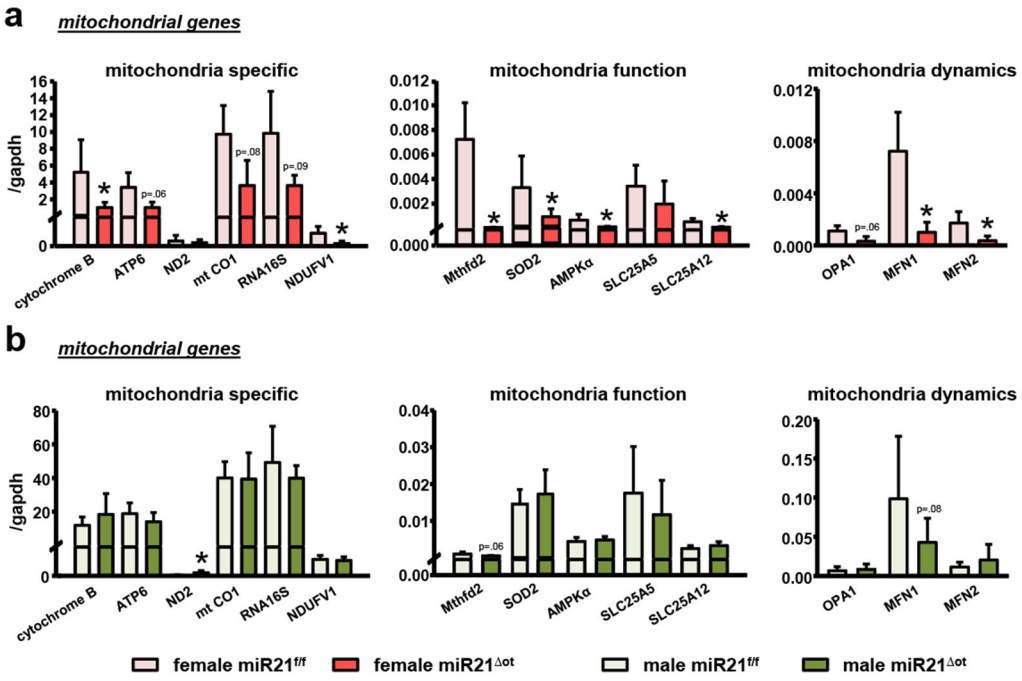

Figure 3. deletion of miR21 from osteocytes differentiatly regulate mitochodrial genes in female and male miR21$^{\Delta ot}$ mice.

mRNA expression of mitochondrial genes in calvaria bones from **(a)** female and **(b)** male miR21$^{f/f}$ and miR21$^{\Delta ot}$ mice (n= 10). Bars represent mean ± s.d., *p<0.05 versus negative control, by t-test.

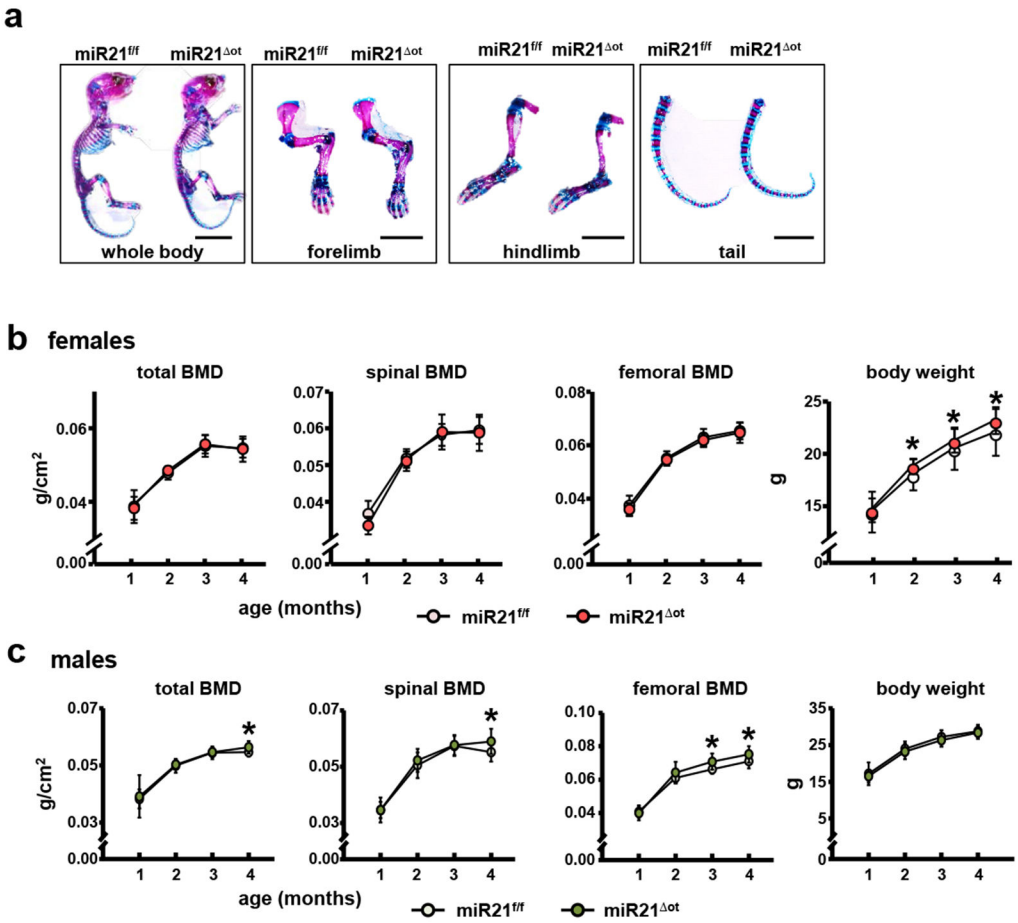

Figure 4. Removal of osteocytic miR21 regulates body weight and bone mass accrual in a sex-dependent manner.

a. Representative images of whole body preparations (n=3/genotype) stained by Alcian blue/alizarin red in 7-day-old mice for evaluation of cartilage (blue) and calcified tissue (magenta). Scale bars indicate 1 cm (for whole body) or 0.5 cm (for forelimb, hindlimb, and tail). Body weight, and total, spinal and femoral BMD (DXA) were assessed monthly from 1 to 4 months of age in **(b)** female and **(c)** male miR21$^{f/f}$ and miR21$^{\Delta ot}$ mice (n=12-16). Bars represent mean ± s.d., *p<0.05 versus miR21$^{f/f}$ at the same age, by t-test.

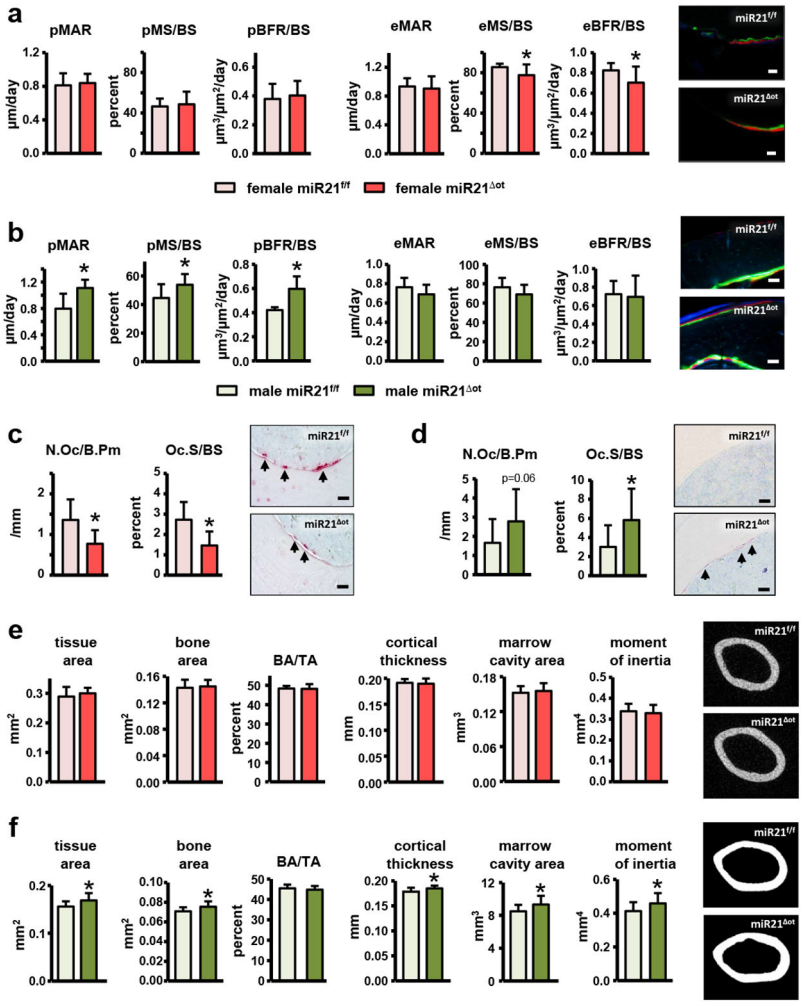

Figure 5. Osteocytic-miR21 deletion leads to sex-specific changes in femoral cortical bone turnover and architecture.

(a-b) Mineral apposition rate (MAR), mineralizing surface (MS)/BS, and bone formation rate (BFR)/BS were measured in unstained cross-sections of the femoral mid-diaphysis on the endosteal and periosteal surfaces of **(a)** female and **(b)** male miR21$^{f/f}$ and miR21$^{\Delta ot}$ mice (n=9-10). Representative fluorescent images are shown, scale bar indicates 25μm. **(c-d)** Osteoclast number (N.Oc)/BS and surface covered by osteoclasts (Oc.S)/BS were scored on the endosteal surface of femoral mid-diaphysis bone sections stained for TRAPase/T. blue of **(c)** female and **(d)** male miR21$^{f/f}$ and miR21$^{\Delta ot}$ mice (n=10). Representative images from osteoclasts on the bone surface (magenta, arrow) are shown, scale bar indicates 25μm. **(e-f)** Cortical bone geometry in the femoral mid-diaphysis of **(e)** female and **(f)** male miR21$^{f/f}$ and miR21$^{\Delta ot}$ mice was assessed by μCT (n=12). Representative reconstructed images are shown. Bars represent mean ± s.d., *p<0.05 versus miR21$^{f/f}$, by t-test.

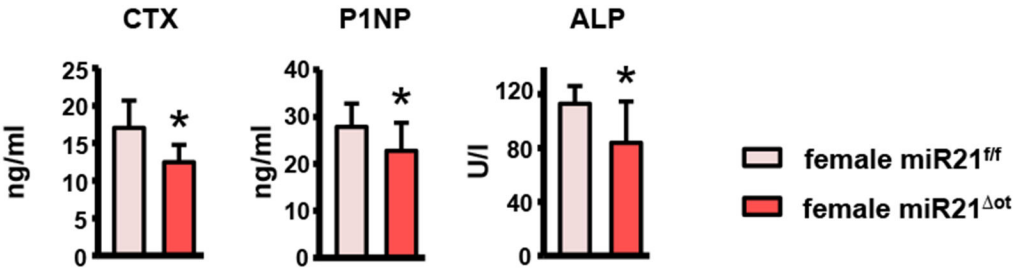

Figure 6. Osteocytic miR21 deficiency suppresses bone turnover in female mice.

Circulating markers of bone resorption (CTX, n=10-15) and formation (P1NP, 10-14 and ALP, n=10-12) measured in serum of 4-month-old female miR21$^{f/f}$ and miR21$^{\Delta ot}$ mice by ELISA.

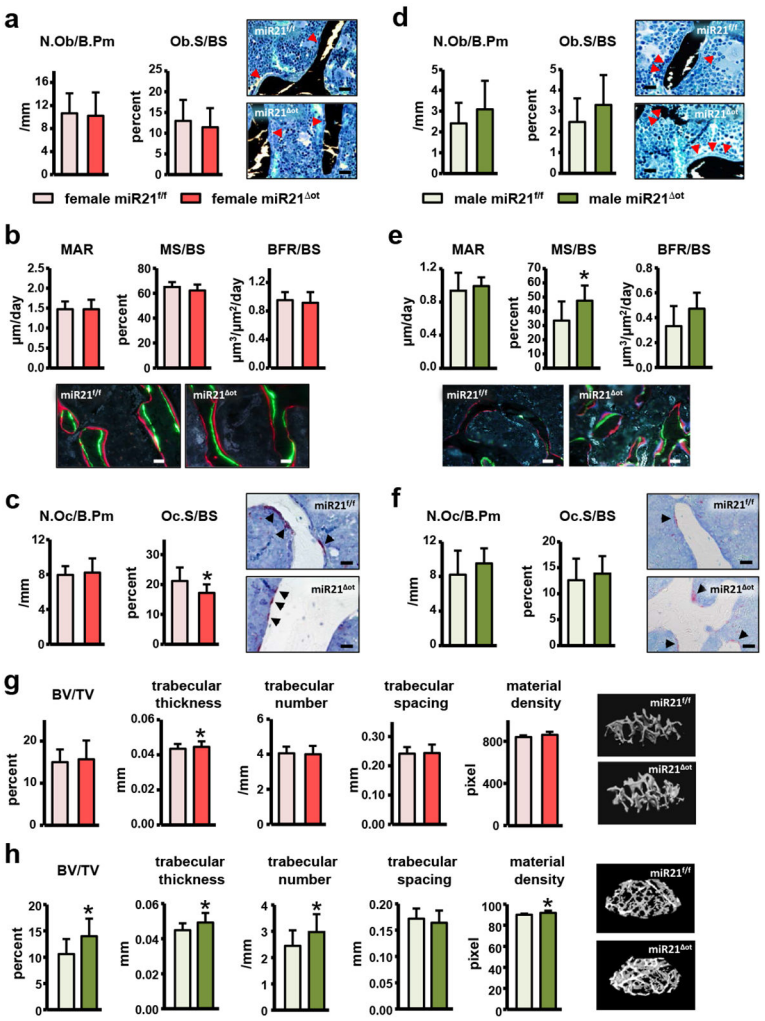

Figure 7. Sex-dependent alterations in vertebral cancellous bone turnover and architecture induced with removal of osteocytic-miR21.

(a-f) Number of osteoblasts (N.Ob)/BS and bone surface covered by osteoblasts (Ob.S)/BS were scored in lumbar vertebra from **(a)** female and **(d)** male miR21$^{f/f}$ and miR21$^{\Delta ot}$ mice bone sections stained with von Kossa/McNeal (n=7-10). Representative images of osteoblasts are shown, scale bar indicates 25μm. Mineral apposition rate (MAR), mineralizing surface (MS)/BS, and bone formation rate (BFR)/BS measured in unstained sections of the lumbar vertebra from **(b)** female and **(e)** male miR21$^{f/f}$ and miR21$^{\Delta ot}$ mice (n=8-10). Representative fluorescent images are shown, scale bar indicates 25μm. Osteoclast number (N.Oc)/BS and surface covered by osteoclasts (Oc.S)/BS were scored on the cancellous bone surface of the lumbar vertebra from **(c)** female and **(f)** male miR21$^{f/f}$ and miR21$^{\Delta ot}$ mice stained for TRAPase/T. blue (n=9-10). Representative images from osteoclasts on the bone surface (magenta, arrow) are shown, scale bar indicates 25μm. **(g-h)** Analysis of cancellous bone microarchitecture in L4 vertebra from **(g)** female and **(h)** male miR21$^{f/f}$ and miR21$^{\Delta ot}$ mice assessed by μCT (n=12-14). Representative 3D images of vertebral cancellous bone are shown. Bars represent mean ± s.d., *p<0.05 versus miR21$^{f/f}$, by t-test.

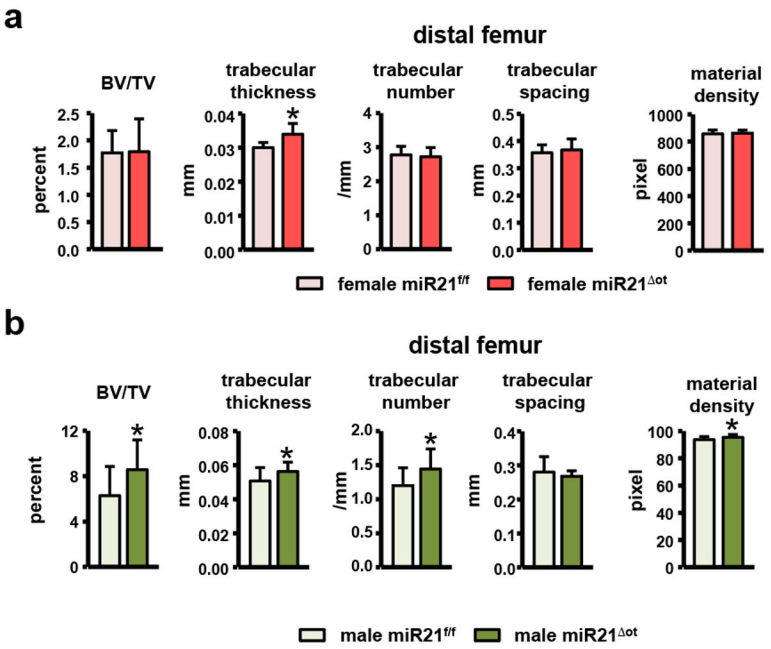

Figure 8. Removal of osteocytic alters distal femur cancellous architecture in a sex-dependent manner.

Analysis of the distal femur cancellous bone microarchitecture of female and male miR21$^{f/f}$ and miR21$^{\Delta ot}$ mice was assessed by μCT (n=12-14). Bars represent mean ± s.d., *p<0.05 versus miR21$^{f/f}$, by t-test.

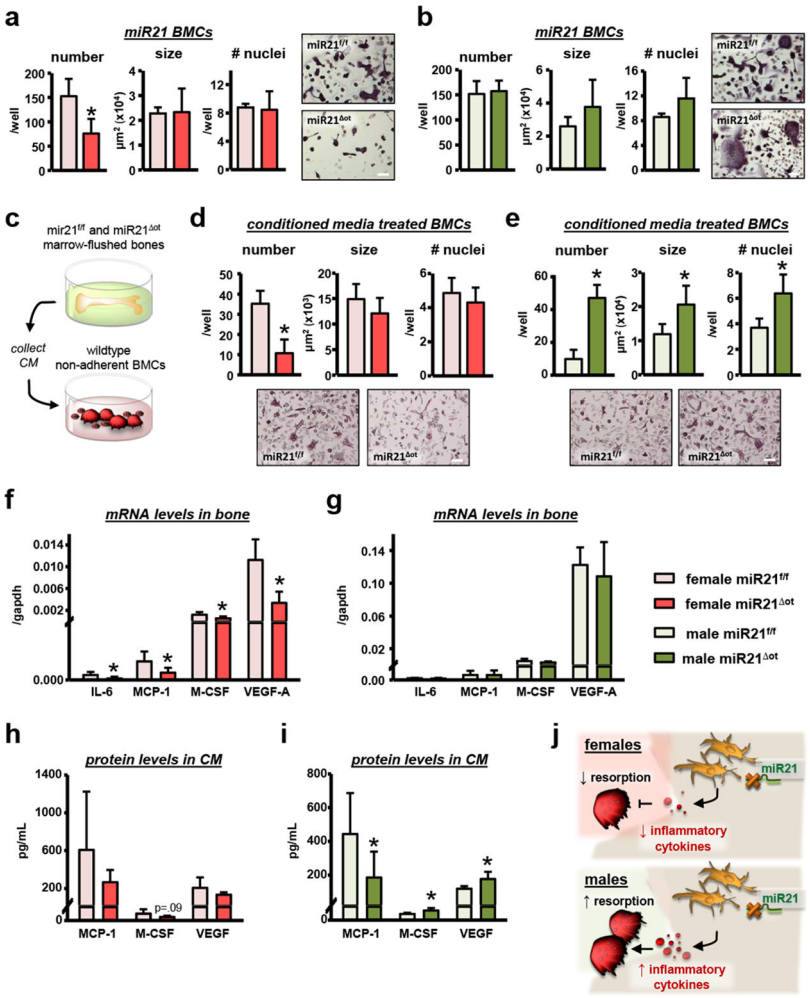

Figure 9. Sex-specific regulation of osteoclast differentiation following osteocytic-miR21 removal.

(a-b) Non-adherent BMCs harvested from female and male miR21$^{f/f}$ and miR21$^{\Delta ot}$ were differentiated into osteoclasts with RANKL/M-CSF for 7 days. Osteoclast number per well, average osteoclast size and number of nuclei per osteoclast were scored for **(a)** female and **(b)** male miR21$^{f/f}$ and miR21$^{\Delta ot}$ non-adherent BMCs (n=4). Representative images from mature osteoclasts stained for TRAPase are shown, scale bar indicates 100μm. **(c)** Illustration of experimental design in which non-adherent BMCs isolated from wild-type C57BL/6 mice were treated with CM from *ex vivo* cultures of long bones from female and male miR21$^{f/f}$ and miR21$^{\Delta ot}$ and supplemented with RANKL/M-CSF for 7 days. **(d-e)** Osteoclast number per well, average osteoclast size and number of nuclei per osteoclast were scored for female non-adherent BMCs treated with CM from **(d)** female and **(e)** male miR21$^{f/f}$ and miR21$^{\Delta ot}$ (n=6). Representative images from mature osteoclasts stained for TRAPase are shown, scale bar indicates 100μm. **(f-g)** mRNA expression of pro-inflammatory cytokine genes in calvaria bones from **(f)** female and **(g)** male miR21$^{f/f}$ and miR21$^{\Delta ot}$ mice. **(h-i)** Pro-inflammatory cytokine protein levels in CM from *ex vivo* marrow-flushed osteocyte enriched bone cultures from **(h)** female and **(i)** male miR21$^{f/f}$ and miR21$^{\Delta ot}$ mice, measured by Milliplex cytokine array. Bars represent mean ± s.d., *p<0.05

versus miR21$^{f/f}$, by t-test. **(J)** Illustration of the proposed model by which removal of osteocytic miR21 modulates pro-inflammatory cytokine production and osteoclast differentiation.

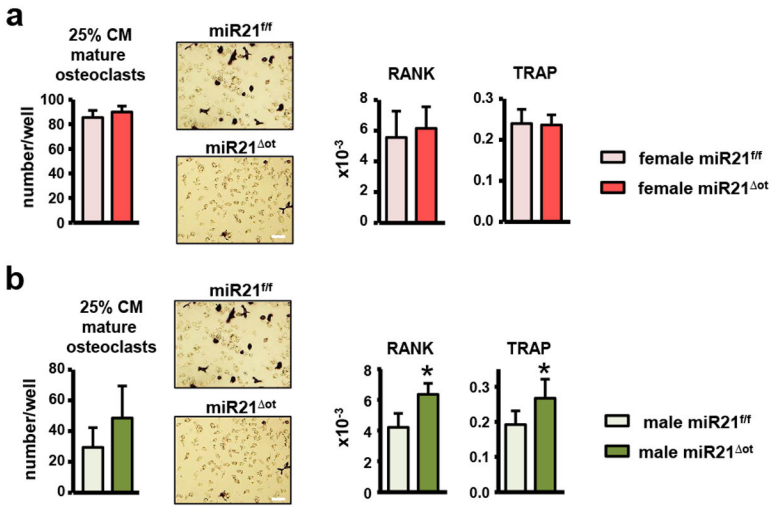

Figure 10. Sex-specific regulation of osteoclast differentiation following osteocytic-miR21 removal.

Osteoclast number per well and gene expression levels were measured in non-adherent BMCs treated with 25% conditioned media from **(a)** female and **(b)** male $miR21^{f/f}$ and $miR21^{\Delta ot}$ (n=6). Bars represent mean ± s.d., *p<0.05 versus $miR21^{f/f}$, by t-test. Representative images from mature osteoclasts stained for TRAPase are shown, scale bar indicates 100μm.

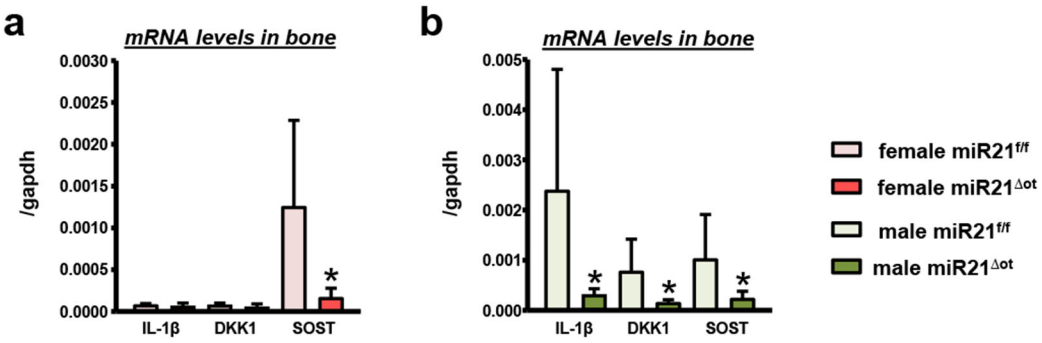

Figure 11. Sex-dependent decreases in anti-osteoblastic cytokine mRNA levels in the absence of osteocytic miR21.

mRNA levels of IL-1β, DKK1, and SOST measured in calvaria bones from **(a)** female and **(b)** male miR21$^{f/f}$ and miR21$^{\Delta ot}$ mice (n=10). Bars represent mean ± s.d., *p<0.05 versus miR21$^{f/f}$, by t-test.

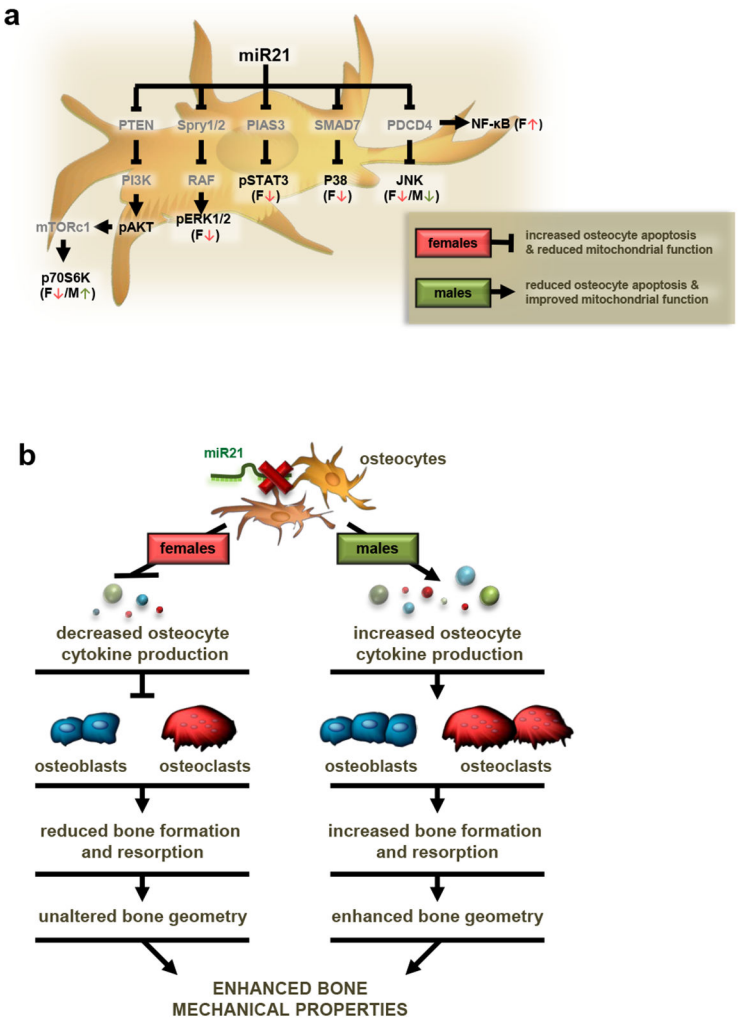

Figure 12. Proposed autocrine and paracrine effects of osteocytic miR21 removal.

(a) Figure illustrating the sex-specific regulation of key cell-signaling pathways in osteocytes by miR21, in turn, leads to sex-dependent alterations in osteocyte viability and mitochondrial function. Previously identified miR21 targets are shown in grey and proteins altered in the current study are shown in black. Direction of changes in protein levels are indicated using arrows for miR21$^{\Delta ot}$ female (pink) and male (green) mice. **(b)** Working model showing the proposed sex-dependent mechanisms by which miR21 regulation in osteocytes alters bone metabolism and geometry through paracrine actions on osteoblasts and osteoclasts. At the same time, removal of osteocytic miR21 enhances bone mechanical properties in a sex-independent manner.

Table 1.

Cytokines in conditioned media from female miR21$^{\Delta ot}$ mice.

	miR21$^{f/f}$	miR21$^{\Delta ot}$	% change	p-value
IL-6	OOR>	OOR>		
Eotaxin	16.63 ± 14.14	6.81 ± 1.52	−59.05	0.12
IFN-g	2.78 ± 0.60	1.88 ± 1.40	−32.43	0.27
IL-1a	19.86 ± 9.73	4.67 ± 4.89	−26.16	0.27
IL-2	OOR<	OOR<		
IL-3	OOR<	OOR<		
IL-4	1.15 ± 0.41	1.00 ± 0.25	−12.88	0.47
IL-5	13.99 ± 6.58	9.66 ± 2.73	−30.94	0.17
IL-7	OOR<	OOR<		
IL-9	133.69 ± 41.57	126.19 ± 22.48	−5.61	0.71
IL-10	5.11 ± 2.24	3.55 ± 1.06	−30.60	0.15
IL-12(p40)	OOR<	OOR<		
IL-12(p70)	13.48 ± 6.96	13.34 ± 4.45	−1.03	0.97
IL-13	OOR<	OOR<		
IL-15	4.05 ± 2.50	6.00 ± 3.53	47.96	0.46
IP-10	117.55 ± 48.07	70.89 ± 49.31	−39.69	0.15
LIF	358.56 ± 202.19	326.44 ± 127.57	−8.96	0.75
LIX	63.85 ± 58.73	40.30 ± 19.16	−36.88	0.37
M-CSF	12.70 ± 8.09	6.7 ± 2.54	−51.44	0.09
MIG	109.53 ± 38.44	86.11 ± 18.64	−21.38	0.21
MIP-1β	48.52 ± 31.58	26.94 ± 5.81	−44.47	0.13
MIP-2	45.33 ± 14.96	44.95 ± 13.45	−0.84	0.97
G-CSF	1127.08 ± 931.54	1026.83 ± 595.91	−8.89	0.83
IL-1β	9.52 ± 6.59	8.66 ± 2.21	−9.15	0.77
IL-17	1.00 ± 0.60	0.91 ± 0.43	−9.47	0.76
KC	379.31 ± 656.65	269.09 ± 302.65	−29.06	0.72
MCP-1	607.36 ± 615.80	264.68 ± 130.32	−56.42	0.21
MIP-1α	36.17 ± 13.52	29.95 ± 6.53	−17.21	0.34
RANTES	OOR<	OOR<		
TNF-α	7.84 ± 6.71	4.28 ± 1.03	−45.39	0.23
GM-CSF	23.13 ± 12.14	19.84 ± 6.10	−14.21	0.57
VEGF	204.67 ± 110.32	132.28 ± 25.83	−35.37	0.15

*p<0.05 versus miR-21$^{f/f}$ mice, by t-test (n=3-6). Values outside the standard curve are denoted by “OOR<” or “OOR>” (Out of Range).

Table 2.

Cytokines in conditioned media from male miR21$^{\Delta ot}$ mice.

	miR21$^{f/f}$	**miR21$^{\Delta ot}$**	**% change**	**p-value**
IL-6	OOR>	OOR>		
Eotaxin	8.22 ± 6.34	6.43 ± 4.13	−21.81	0.57
IFN-g	2.70 ± 0.58	2.54 ± 1.05	−6.06	0.75
IL-1a	15.90 ± 2.24	13.06 ± 4.64	−17.88	0.21
IL-2	OOR<	OOR<		
IL-3	OOR<	OOR<		
IL-4	0.94 ± 0.20	0.82 ± 0.13	−13.25	0.23
IL-5	8.55 ± 2.52	6.01 ± 1.69	−29.77	0.07
IL-7	OOR<	OOR<		
IL-9	122.17 ± 18.99	142.73 ± 18.89	16.84	0.09
IL-10	4.88 ± 3.10	3.37 ± 0.82	−30.94	0.28
IL-12(p40)	OOR<	OOR<		
IL-12(p70)	16.24 ± 3.16	14.74 ± 4.05	−9.29	0.49
IL-13	OOR<	OOR<		
IL-15	3.78 ± 2.44	5.80 ± 6.45	53.63	0.53
IP-10	46.00 ± 17.06	76.65 ± 57.81	64.44	0.26
LIF	432.25 ± 99.60	422.48 ± 178.49	−2.26	0.91
LIX	61.89 ± 14.19	41.35 ± 20.70	−33.19	0.07
M-CSF	**4.45 ± 0.97**	**7.11 ± 1.81**	**59.64** *	**0.01**
MIG	75.46 ± 18.73	83.83 ± 26.69	11.10	0.54
MIP-1β	27.84 ± 5.88	23.54 ± 1.77	−15.44	0.12
MIP-2	56.2 ± 16.81	38.11 ± 12.07	−32.19	0.06
G-CSF	1576.48 ± 377.85	1029.03 ± 1013.82	−34.73	0.24
IL-1β	9.56 ± 3.46	9.75 ± 2.73	1.99	0.92
IL-17	1.14 ± 0.23	1.04 ± 0.48	−9.20	0.64
KC	269.79 ± 160.04	97.42 ± 99.26	−63.89	0.06
MCP-1	**443.16 ± 243.87**	**184.39 ± 154.34**	**−58.39**	**0.05**
MIP-1α	29.1 ± 3.34	28.18 ± 3.75	−53.15	0.66
RANTES	OOR<	OOR<		
TNF-α	4.48 ± 0.34	4.29 ± 0.57	−4.17	0.50
GM-CSF	24.80 ± 3.05	21.60 ± 6.18	−12.88	0.28
VEGF	**117.78 ± 15.83**	**176.17 ± 42.68**	**49.58** *	**0.01**

* $p<0.05$ versus miR-21$^{f/f}$ mice, by t-test (n=5-6). Values outside the standard curve are denoted by “OOR<” or “OOR>” (Out of Range).

Table 3.

Phosphorylated/total protein levels measured by 9-Plex cell-signaling array in bones from female miR21$^{\Delta ot}$ mice.

	miR21$^{f/f}$	**miR21$^{\Delta ot}$**	**% change**	**p-value**
CREB	0.012 ± 0.002	0.012 ± 0.005	0.56	0.98
JNK	**0.390 ± 0.123**	**0.298 ± 0.04**	**−35.44**	**0.03**
NF-κB	0.024 ± 0.002	0.030 ± 0.005	22.68	0.06
ERK 1/2	**0.034 ± 0.009**	**0.021 ± 0.006**	**−37.81**	**0.03**
AKT	0.851 ± 0.297	0.745 ± 0.158	−12.54	0.49
P70S6K	0.245 ± 0.054	0.209 ± 0.041	−14.52	0.23
STAT3	**0.055 ± 0.013**	**0.040 ± 0.011**	**−27.65**	**0.05**
STAT5	0.577 ± 0.121	0.576 ± 0.086	−0.253	0.98
P38	**0.533 ± 0.071**	**0.392 ± 0.113**	**−26.48**	**0.03**

* $p<0.05$ versus miR-21$^{f/f}$ mice, by t-test (n=5-6)

Table 4.

Phosphorylated/total protein levels measured by 9-Plex cell-signaling array in bones from male miR21$^{\Delta ot}$ mice.

	miR21$^{f/f}$	miR21$^{\Delta ot}$	% change	p-value
CREB	0.011 ± 0.005	0.011 ± 0.002	−0.76	0.97
JNK	0.424 ± 0.128	0.295 ± 0.089	−27.58	0.11
NF-κB	0.028 ± 0.006	0.028 ± 0.006	−1.29	0.92
ERK 1/2	0.037 ± 0.017	0.031 ± 0.009	−16.22	0.46
AKT	0.610 ± 0.085	0.605 ± 0.088	−0.79	0.93
P70S6K	**0.241 ± 0.045**	**0.294 ± 0.028**	**21.87**	**0.04**
STAT3	0.046 ± 0.018	0.050 ± 0.010	8.08	0.67
STAT5	0.585 ± 0.155	0.526 ± 0.041	−10.02	0.39
P38	0.540 ± 0.127	0.575 ± 0.122	6.37	0.64

* $p<0.05$ versus miR-21$^{f/f}$ mice, by t-test (n=5-6)

Table 5.

Mechanical strength in cortical bone in female miR21$^{\Delta ot}$ mice.

	miR21$^{f/f}$	**miR21$^{\Delta ot}$**	**% change**
Yield Force (N)	8.978 ± 0.602	8.66 ± 0.486	−3.53
Ultimate Force (N)	11.662 ± 1.013	11.628 ± 1.168	−0.29
Pre-Yield Displacement (μm)	215.073 ± 22.801	221.153 ± 23.920	2.83
Post-yield Displacement (μm)	981.928 ± 380.192	**1328.576 ± 292.795** *	35.30
Total Displacement (μm)	1197.002 ± 376.015	**1549.729 ± 285.952** *	29.47
Stiffness (N/mm)	47.874 ± 6.39	45.632 ± 4.105	−4.68
Pre-yield Work (mJ)	1.049 ± 0.171	1.019 ± 0.1349	−2.82
Post-yield Work (mJ)	8.200 ± 1.991	**9.791 ± 1.303** *	19.40
Total Work (mJ)	9.249 ± 1.910	**10.811 ± 1.298** *	16.88
Yield Stress (MPa)	36.905 ± 4.038	35.253 ± 4.983	−4.48
Ultimate Stress (MPa)	47.798 ± 4.570	47.076 ± 5.806	−1.51
Pre-yield Strain (με)	19432.98 ± 1646.98	19533.12 ± 2215.71	0.52
Total Strain (με)	108546.8 ± 34714.9	**137001.5 ± 27440.5** *	26.21
Modulus (GPa)	2.156 ± 0.195	2.094 ± 0.239	−2.89
Resilience (MPa)	0.391 ± 0.077	0.368 ± 0.080	−5.74
Toughness (MPa)	3.449 ± 0.818	3.875 ± 0.660	12.33

* $p<0.05$ versus miR-21$^{f/f}$ mice, by t-test (n=10-12)

Table 6.

Mechanical strength in cortical bone in male miR21$^{\Delta ot}$ mice.

	miR21$^{f/f}$	**miR21$^{\Delta ot}$**	**% change**
Yield Force (N)	11.086 ± 1.858	10.032 ± 2.292	−9.51
Ultimate Force (N)	13.039 ± 1.500	13.507 ± 1.276	3.59
Pre-Yield Displacement (μm)	306.050 ± 57.920	**257.687 ± 50.334** *	−15.80
Post-yield Displacement (μm)	511.277 ± 191.202	**992.232 ± 372.887** *	94.07
Total Displacement (μm)	786.897 ± 124.494	**1260.106 ± 366.007** *	60.14
Stiffness (N/mm)	42.591 ± 4.177	44.465 ± 4.182	4.40
Pre-yield Work (mJ)	1.654 ± 0.533	1.249 ± 0.538	−24.49
Post-yield Work (mJ)	5.563 ± 1.693	**9.537 ± 2.676** *	71.43
Total Work (mJ)	6.981 ± 1.325	**10.879 ± 2.793** *	55.83
Yield Stress (MPa)	84.042 ± 14.228	**70.200 ± 17.563** *	−16.47
Ultimate Stress (MPa)	98.449 ± 7.539	94.338 ± 7.406	−4.18
Pre-yield Strain (με)	44489.068 ± 8781.447	38232.606 ± 7489.234	−14.06
Total Strain (με)	119759.5 ± 24724.3	**186827.1 ± 56494.9** *	56.00
Modulus (GPa)	2.237 ± 0.163	2.067 ± 0.299	−7.62
Resilience (MPa)	1.813 ± 0.545	**1.037 ± 0.272** *	−42.78
Toughness (MPa)	9.095 ± 3.038	**11.635 ± 2.375** *	27.92

* $p<0.05$ versus miR-21$^{f/f}$ mice, by t-test (n=10-12).